Paired organic matter and pyrite $\delta^{34}S$ records reveal mechanisms of carbon, sulfur, and iron cycle disruption during Ocean Anoxic Event 2

Morgan Reed Raven[*a,b], David A. Fike [b], Alexander S. Bradley [b]; Maya L. Gomes [c], Jeremy D. Owens [d], Samuel A. Webb [e]

[a] *Dept. of Earth Sciences, University of California, Santa Barbara, CA 93130 USA*
[b] *Dept. of Earth and Planetary Sciences, Washington University in St Louis, MO 63130*
[c] *Dept. of Earth and Planetary Sciences, Johns Hopkins University, Baltimore, MD 21218*
[d] *Dept. of Earth, Ocean, and Atmospheric Science, Florida State University, Tallahassee, FL 32306*
[e] *Stanford Synchrotron Radiation Lightsource, Stanford University, Menlo Park, CA, 94025*
* = *corresponding author, raven@ucsb.edu*

Abstract

Sulfur (S) isotope compositions of pyrites in the sedimentary record have played an important part in our understanding of biogeochemical cycling in the geologic record. However, the kinetics of pyritization are complex and depend strongly on the reactivity and mineralogy of available iron. As a second major sink for sulfide in anoxic sediments, organic matter (OM) provides essential context for reconstructing the distribution and isotopic composition of environmental sulfide. To first order, roughly parallel pyrite and OM $\delta^{34}S$ profiles reflect changes in sulfide, while independent patterns require alternative explanations, including changes in iron availability or OM characteristics. We apply this framework to Ocean Anoxic Event 2 (OAE-2, 94 Mya), a period of enhanced reduced C and S burial (in OM and pyrite) that was associated with expanded marine anoxia. We present paired S-isotope records for pyrite and OM along with profiles of OM S:C ratio and S redox speciation from four well-characterized lithologic sections (Pont d'Issole, Cismon, Tarfaya Basin, and Demerara Rise) to reconstruct both local redox structure and global mechanisms impacting the C, S and Fe cycles around OAE-2.

OM sulfurization appears to be a major control on OM preservation at all four sites. Similar to modern anoxic environments, there is a positive correlation between OM S:C ratios and OM concentrations for sites with more reducing conditions, implying a link between OM sulfurization and burial. At consistently anoxic sites like Tarfaya Basin and Demerara Rise, strongly sulfurized OM with a consistent S redox speciation and S-isotope composition most likely formed rapidly in sinking particles before, during, and after OAE-2. Particle-hosted OM sulfurization may therefore have been a central mechanism facilitating the

massive burial of OM in anoxic environments during this and other periods of enhanced global carbon burial. At the same time, a nearly 25‰ negative shift in the $\delta^{34}S$ values of pyrite – but not OM – occurs at multiple, globally distributed sites near the onset of OAE-2, indicating slower pyritization reactions that likely reflect changes in iron delivery due to expanding regional or global anoxia. The combination of pyrite and organic S isotopes thus provides novel constraints on the interwoven cycles of carbon, iron, and sulfur across a major carbon cycle perturbation.

Introduction

Ocean Anoxic Event 2 (OAE-2, also termed the Cenomanian–Turonian Boundary Event) was a period of dynamic changes in the global carbon cycle in the Cretaceous (~94 million years ago, Mya) during which a large portion of the global ocean experienced anoxia (Ostrander et al., 2017) and associated biological turnover (Keller et al., 2008) and refs therein). Expanded euxinia at the onset of the event contributed to the preservation of extraordinary amounts of organic matter (OM) in marine sediments, equivalent to roughly a 60 to 80% increase in the global flux maintained for ~500,000 years (Owens et al., 2013; 2018; Sageman et al., 2006). This burst of ^{13}C-depleted OM preservation generated the characteristic positive C-isotope excursion for OAE-2 and substantially drew down atmospheric CO_2 (Jarvis et al., 2011). OM sulfurization can enhance the preservation of OM under anoxic conditions (Boussafir et al., 1995) and has been described in TOC–rich (>10 wt%) OAE-2 shales (Hetzel et al., 2009; Kolonic et al., 2002) as well as in interbedded carbonates and marly shales with more moderate (0.2–3 wt%) TOC (Raven et al., 2018). Still, it remains difficult to quantify the impact of sulfurization on OM preservation under

different environmental conditions, much less to extrapolate to global fluxes of reduced sulfur and carbon burial or to estimate how those fluxes might change before, during, and after OAE-2.

Primary considerations for determining the significance of sulfurization for C fluxes are the rates and locations of S cycling in the environment. Two distinct timescales of sulfurization reactions occur in modern environments: gradual sulfurization reactions between bisulfide (HS^-) and relatively recalcitrant OM occur over thousands of years under strongly reducing conditions (Werne et al., 2000), and rapid sulfurization reactions between polysulfides (S_x^{2-}) and relatively fresh, labile OM occur on timescales of days near dynamic redox interfaces, for example in sinking particles (Raven et al., 2016a). Rapid sulfurization has the potential to impact a much larger pool of OM and have a much more dramatic impact on C fluxes (Raven et al., 2018).

S–isotope ratios (expressed as $\delta^{34}S$ values) are powerful tools for reconstructing the sources of sulfide in the environment as well as its various potential sinks, including reoxidation or precipitation as either abiogenic OM or pyrite (FeS_2). Near the onset of OAE-2, previously published S-isotope profiles of pyrite from multiple sites show intriguing shifts toward ^{34}S-depleted values that have been interpreted in terms of changing marine sulfate concentrations (Adams et al., 2010), local chemocline position (Gomes et al., 2016), and the extent of oxidative microbial sulfur cycling (Hetzel et al., 2009; Kolonic et al., 2002). Although each of these hypotheses invoke changes in the distribution or $\delta^{34}S$ value of sulfide in the environment, OAE-2 is also associated with major changes in iron

cycling due to inputs from active rifting and volcanism (Owens et al., 2012), which could also impact pyrite $\delta^{34}S$ values via changes in iron distributions and mineralogy. To distinguish among these possibilities, we integrate pyrite $\delta^{34}S$ records with OM $\delta^{34}S$ values and S speciation data from four OAE-2 sections located in different parts of the Tethys and proto–North Atlantic Oceans. Our results indicate that the strong negative shift in pyrite $\delta^{34}S$ values from globally dispersed sites likely reflects a change in the quantity or speciation of iron delivery to these locations. We also find evidence for a generalizable relationship between sulfurization intensity and OM preservation in sediments, which implies that OM sulfurization can be a primary driver of changes in C burial during OAE-2 and throughout Earth history.

Methods Summary

Samples were prepared from previously sampled sections by sequential extraction (Canfield et al., 1986; Raven et al., 2018). Powdered rock samples were washed with DI water, lyophilized, and microwave–extracted twice with organic solvents (9:1 dichloromethane:methanol, MARS6, CEM Corp.) prior to chromium reduction (6N HCl + $CrCl_2$, 180°C, 4 hrs) and trapping of released sulfide as ZnS in 5% zinc acetate solution. The microwave extraction step removed organic-solvent soluble S, which was not further analyzed for this study. The S liberated by chromium reduction is an operationally-derived pool of metal sulfides, typically considered to be primarily composed of pyrite, and thus will be referred to as 'pyrite' here. Washed ZnS solids from the chromium reduction were oxidized with 30% H_2O_2 (24°C, 24 hrs), quantified as sulfate by ion chromatography (Metrohm 881 ion chromatograph with a Metrosep A Supp 7 150 x 4.0 mm anion column)

and then precipitated as $BaSO_4$ with barium chloride for S-isotope analysis by combustion EA-IRMS (Costech 4010 EA coupled to a Thermo Delta V Plus, configured for S). Remaining solids after chromium reduction were also analyzed by EA-IRMS for S concentrations and $\delta^{34}S$ values. Organic C concentrations and $\delta^{13}C$ values were measured using a Thermo Flash 2000 EA with zero-blank autosampler coupled to a Delta V Plus, configured for C. All C- and S-isotope ratio measurements were made at Washington University in St Louis and are reported in per mil (‰) units relative to VPDB and VCDT, respectively. Unconsolidated sediments from a recent (160,000 – present) core from the TOC-lean Gulf of Lion (northwestern Mediterranean, borehole PRGL1–4, https://www.pangaea.de/?q=PROMESS1) were prepared according to the same methods for comparison below. Residual solids were also analyzed for organic S speciation by x-ray absorption spectroscopy on beamline 14–3 at the Stanford Synchrotron Radiation Lightsource (SSRL) at the SLAC National Accelerator Laboratory. Spectra were collected for each sample using a ~500 x 1000 μm beam with a flux of 2 x 10^{10} photons/sec, calibrated to the thiosulfate ($Na_2S_2O_3$) pre-edge peak at 2472.02 eV. Spectra were processed and fit using a set of in-house standards with the SIXPACK software package (Webb, 2005).

Study Sites and Results

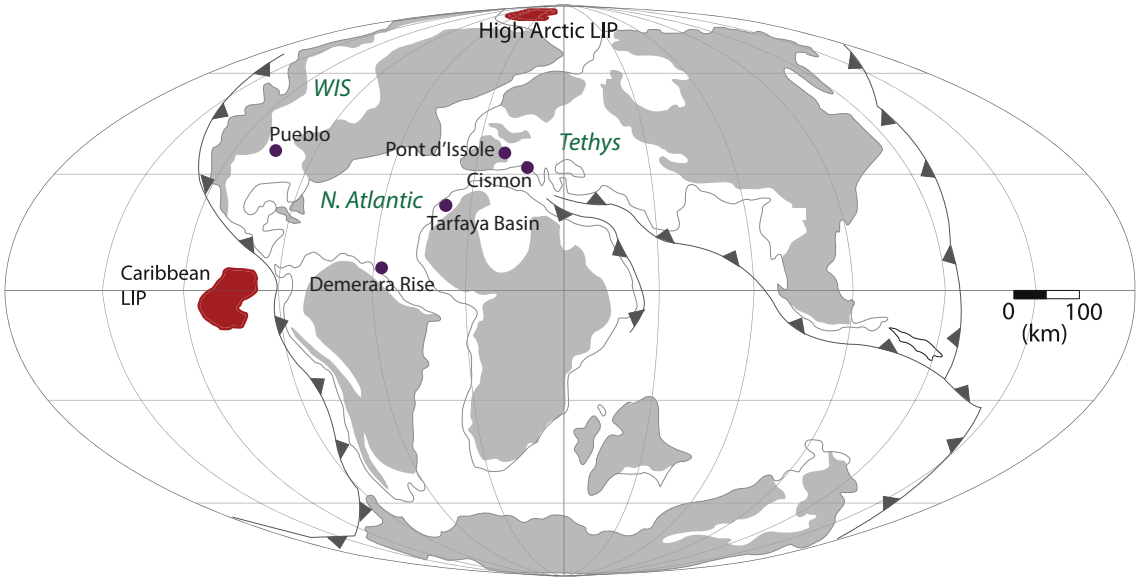

126

127 **Fig. 1 Paleo-geography of study sites during OAE-2.** Map is modified from (du Vivier
128 et al., 2014) with study sections marked by purple circles. Locations of Large Igneous
129 Provinces (LIP) are also shown in red.

130

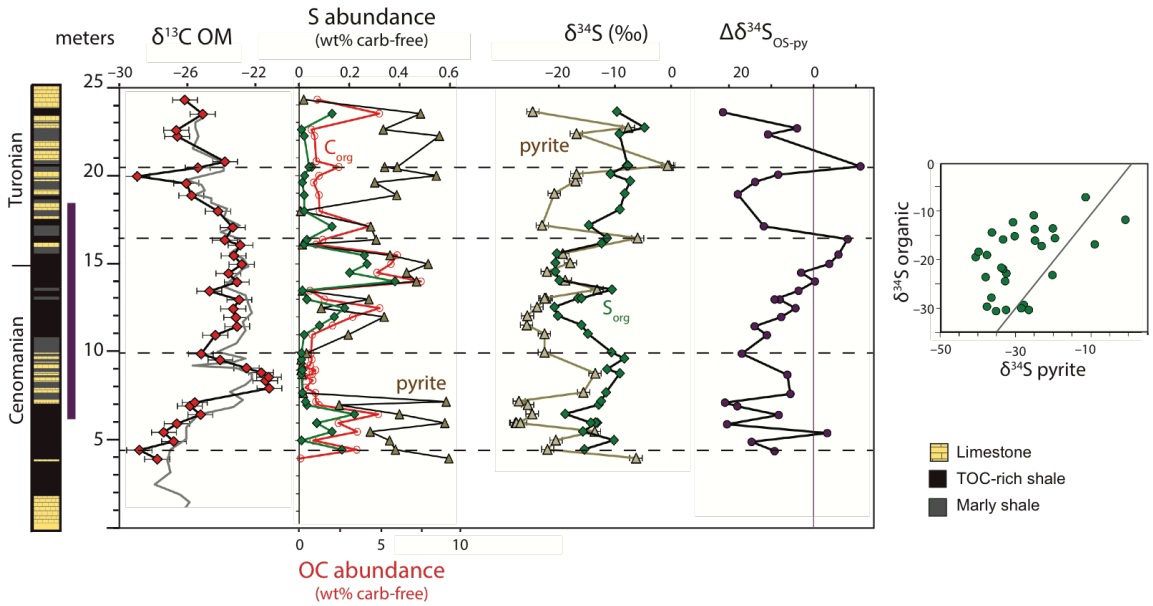

131

132 **Fig. 2 Pont d'Issole record.** The purple bar at left represents the interpreted duration of
133 OAE-2 based on the C-isotope excursion. The grey line for $\delta^{13}C_{OM}$ is from (Jarvis et al.,

2011), and lithology is from (Gomes et al., 2016). Dashed horizontal lines are intended as visual aids to highlight patterns in the records. Vertical purple line for $\Delta\delta^{34}S_{OS\text{-}py}$ shows $\delta^{34}S_{pyrite} = \delta^{34}S_{OS}$. Grey line in the right-hand panel shows a 1:1 line.

The Pont d'Issole section was deposited in a subsiding basin within the northern Tethys Ocean (~30°N, Fig. 1) in several hundred meters of water depth with an average sedimentation rate of roughly 2.4 cm/yr (12-m-thick C-isotope excursion, ~500 kyr, (Jarvis et al., 2011)). This section is characterized by recurrent shifts in lithology and OM concentration between relatively OM-lean (<0.2 wt% TOC) limestones and relatively OM-rich (>1.0 wt% TOC) shales and marly shales (Gomes et al., 2016). Shale layers contain relatively S-rich and ^{34}S-depleted OM, indicating early OM sulfurization during shale deposition under more O_2-limited conditions (Raven et al., 2018). The pyrite $\delta^{34}S$ record from our Pont d'Issole sample set (Fig. 2; cf. (Gomes et al., 2016)) has many similarities to the OM $\delta^{34}S$ record, with comparable shifts toward lower $\delta^{34}S$ values in shales before and during the OAE-2 C-isotope excursion. There are also instances, however, where the S-isotope composition of pyrite behaves independently from OM: at 5.5 m and 20.5 m, for example, pyrite is locally strongly ^{34}S-enriched without any parallel excursion in OM $\delta^{34}S$. Additionally, the $\delta^{34}S$ offset between pyrite and organic matter (Fig. 2, $\Delta\delta^{34}S_{OS\text{-}py}$) decreases systematically from 17.4 to –7.9‰ across the duration of the C-isotope excursion. OM and pyrite $\delta^{34}S$ values thus show significant spread around and to the left of the 1:1 line in the cross-plot in Figure 2.

156 At Cismon, a narrow, ~35-cm-thick layer of OM-rich (6.5 – 21.4 wt% TOC) black shale
157 corresponds to part of the OAE-2 C-isotope excursion, although major portions of the C-
158 isotope excursion are absent due to hiatuses (Gambacorta et al., 2015; Gomes et al., 2016).
159 On either side of this lithologic unit, corresponding to the Bonarelli Layer, rocks from
160 Cismon are bedded layers of OM-lean (≤ 0.05 wt% TOC), micritic foraminiferal
161 limestones with occasional cherts and grey shales (Bellanca et al., 1996a; Gambacorta et
162 al., 2015). Unfortunately, these limestones are generally too OM-lean and silicate-rich to
163 permit spectroscopic analysis of S speciation or isotopic analysis of organic S by
164 conventional EA-IRMS. For a point of comparison with OAE-2 shales, we analyzed a
165 selection of limestones with 0.1–0.7 wt% TOC from lower in the section, representing
166 approximately 96 – 100 Mya (spanning a 20-meter-thick zone from 37.5 m above the OAE-
167 1a C-isotope excursion to 20 m below the onset of OAE-2). In both the TOC-rich layer and
168 earlier TOC-lean limestones, OM from Cismon is strongly ^{34}S-depleted, with $\delta^{34}S$ values
169 averaging –37‰ during OAE-2 and –38.8‰ in the earlier samples. Pyrite is also very
170 strongly ^{34}S-depleted throughout the section, averaging –42.7‰ during OAE-2 and –49‰
171 in the earlier samples (Gomes et al., 2016).
172

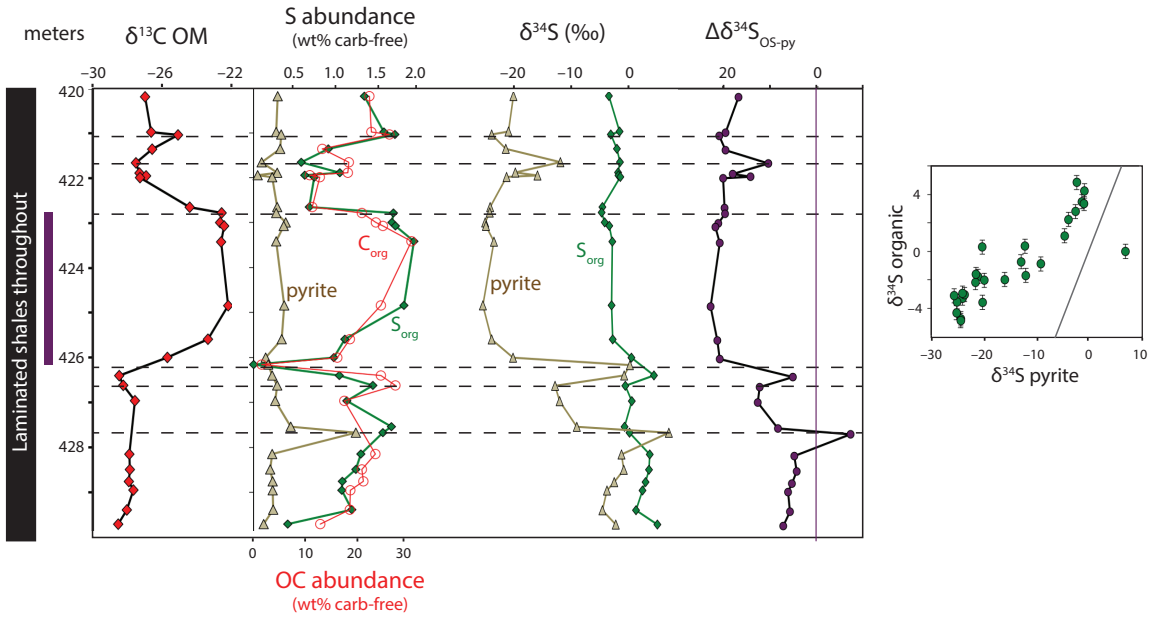

Fig. 3 Demerara Rise record. The purple bar at left represents the interpreted duration of OAE-2 based on the C-isotope excursion. Dashed horizontal lines are intended as visual aids to highlight patterns in the records. Vertical purple line for $\Delta\delta^{34}S_{OS\text{-}py}$ shows $\delta^{34}S_{pyrite} = \delta^{34}S_{OS}$. Grey line in the right-hand panel shows a 1:1 line.

Sediments from Demerara Rise (ODP 1258, using modified composite depths after (Erbacher et al., 2005)) were deposited in the western tropical proto-North Atlantic Ocean and are generally described as laminated OM-rich marl to black shales throughout the investigated section, with an apparent average sedimentation rate of ~0.8 cm/kyr for the 3.5-m-thick C-isotope excursion (Owens et al., 2016). On a carbonate-free basis, concentrations of OM, organic S, and pyrite S are largely invariant across the onset and termination of the OAE. Due to reduced carbonate concentrations during the C-isotope excursion, there is a perceived increase in pyrite and OM concentrations across this interval on a whole-rock basis ((Hetzel et al., 2009); Supplemental Fig. 1). Sediments are extremely

188 OM-rich (Erbacher et al., 2005; Hetzel et al., 2009), containing an average of 24 wt%
189 organic C (Fig. 3, (Owens et al., 2016)) and 4.1 wt% organic S on a carbonate-free basis.
190 These concentrations of organic S exceed those of pyrite S by roughly five times. OM $\delta^{34}S$
191 values are also broadly invariant; samples after the onset of the OAE are slightly more ^{34}S-
192 depleted, but all OM $\delta^{34}S$ values fall in a relatively narrow range between –4.9‰ and
193 +4.8‰. In contrast, pyrite $\delta^{34}S$ values decline substantially across the 2 m of section
194 leading up to the onset of OAE-2, from around –3‰ to around –25‰, in agreement with
195 previously published data (Hetzel et al., 2009). Pyrite S-isotopes are relatively stable at
196 these moderately ^{34}S-depleted compositions throughout the OAE-2 C-isotope excursion
197 and recover partly after the termination of the event. Accordingly, $\Delta\delta^{34}S_{OS\text{-}py}$ at Demerara
198 Rise increases from ~6‰ prior to OAE-2 to ~21‰ during the OAE-2 C-isotope excursion,
199 and the slope of the data in a pyrite–OM $\delta^{34}S$ crossplot is much shallower than the 1:1 line.
200 Like at Pont d'Issole, there are also instances of locally ^{34}S-enriched pyrite without similar
201 enrichment in OS (e.g., 427.7 m).
202

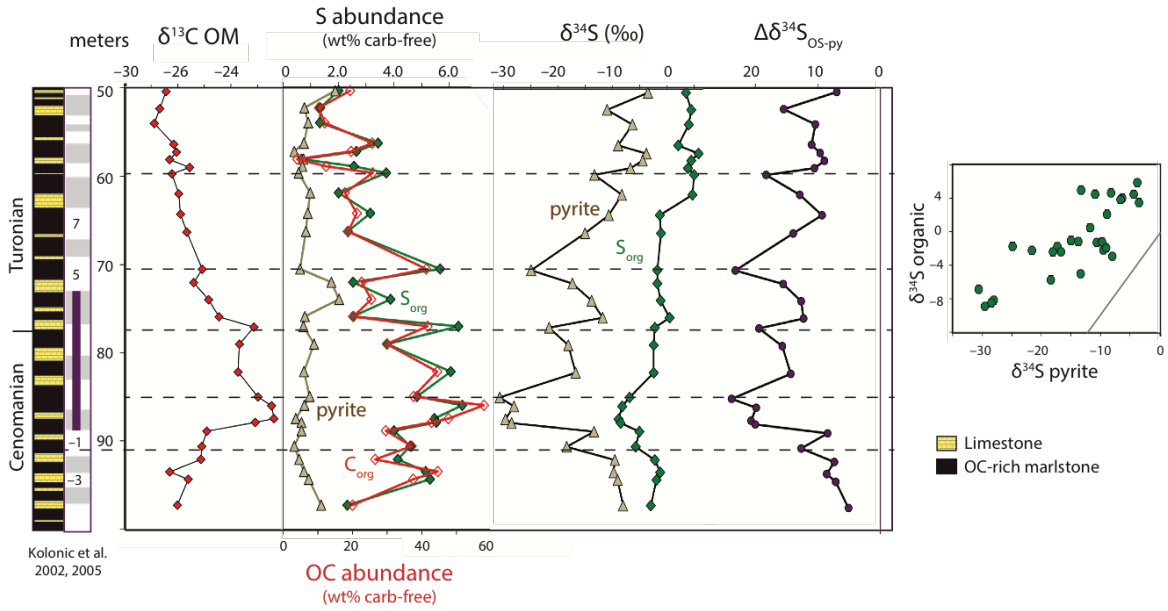

Fig. 4 Tarfaya Basin record. Lithology is shown at left, paired with recurrent sedimentary cycles from Kolonic (2002, 2005). Dashed horizontal lines indicate depths with relatively abundant OM and ^{34}S-depleted pyrite. The purple bar at left represents the interpreted duration of OAE-2 based on the C-isotope excursion. Vertical purple line for $\Delta\delta^{34}S_{OS\text{-}py}$ shows $\delta^{34}S_{pyrite} = \delta^{34}S_{OS}$. Grey line in the right-hand panel shows a 1:1 line.

Tarfaya Basin sediments (sampled from Shell exploration core S75) were deposited on the outer shelf of northwest Africa during a series of transgressive cycles associated with rifting of the southern North Atlantic Basin. High productivity and high sedimentation rates (averaging ~3.3 cm/kyr across the 16.5-meter-thick C-isotope excursion; (Kolonic et al., 2005)) supported the formation of extremely OM-rich black shales and somewhat less OM-rich carbonates, which alternate on apparently orbital timescales (Kolonic et al., 2005; 2002; Poulton et al., 2015) (Fig. 4). This variation is also apparent in the $\delta^{34}S$ profile of pyrite, which is consistent with lower resolution data from (Kolonic et al., 2002) and

Böttcher et al. (unpublished) as reported in (Hetzel et al., 2009). Although we do not have the sampling density to resolve individual orbital cycles, OM-rich layers generally contain relatively ^{34}S-depleted pyrite, as highlighted in dashed lines in Fig. 4. On top of this regular variation, the S-isotope profiles for OM and pyrite have key similarities to those from Demerara Rise. OM and pyrite $\delta^{34}S$ values prior to the onset of the OAE are between 0 and –10‰. By the onset of the OAE-2 C-isotope excursion, pyrite $\delta^{34}S$ values are at their minimum, generally –30‰. In the upper part of the core (depths < 65 m), post-OAE, pyrite $\delta^{34}S$ values return to pre-excursion values (–5 to –10‰). OM $\delta^{34}S$ values express a muted drop from near –2‰ to a minimum of –8.9‰ at the onset of OAE-2 and a gradual increase thereafter, reaching ~4‰ in the top of the section.

Table 1. Average relative abundances of organic S moieties for sections spanning OAE-2 by XAS

			Sulfides		Disulfides		Aromatic S		Sulfoxides		Sulfonates		Sulfate Esters	
Site	**#**	**S:C**	mean	1 s.d.	mean	1 s.d.	mean	1 s.d.	mean	1 s.d.	mean	1 s.d.	mean	1 s.d.
Demerara Rise	24	5.9%	64%	3%	23%	2%	2%	1%	4%	1%	6%	2%	1%	1%
Tarfaya Basin	23	5.0%	59%	3%	14%	3%	14%	1%	4%	1%	8%	1%	0%	0%
Pont d'Issole (S:C >3%)	10	4.3%	57%	3%	17%	2%	15%	2%	3%	1%	8%	2%	0%	1%
Cismon	4	4.8%	52%	2%	16%	2%	20%	1%	4%	1%	7%	1%	1%	0%
Pont d'Issole (S:C <3%)	13	2.2%	42%	8%	22%	8%	16%	8%	3%	2%	11%	7%	5%	5%

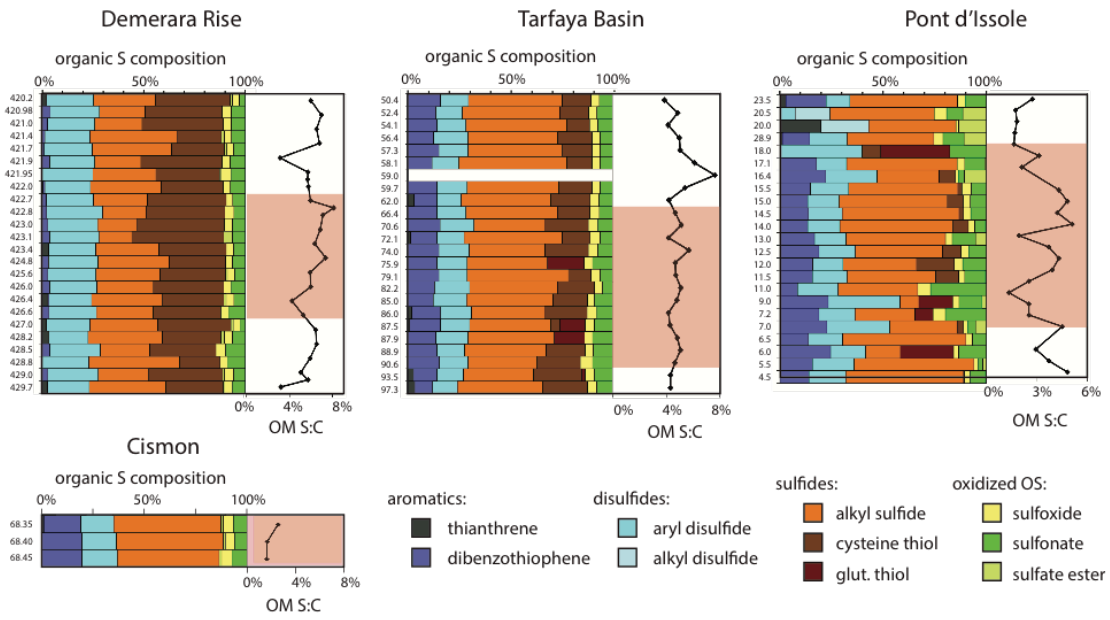

232

233 **Fig. 5: Organic S speciation in organic matter.** XAS and organic matter S:C (mol/mol)
234 ratios show consistent OS redox speciation among Demerara, Tarfaya, and Cismon
235 samples and variable OS redox speciation associated with local environmental change in
236 Pont d'Issole. The red shaded intervals correspond to the OAE-2 C-isotope excursion at
237 each site. Categories of reduced S structures (aromatic, disulfide, and sulfide) can be
238 confidently distinguished, but specific identifications within these groups (e.g., between
239 sulfides and thiols) are tentative.

240

241 X-ray absorption spectroscopy was used to quantify the relative contributions of different
242 forms of organic S to the total solvent– and acid–insoluble OM pool (Eglinton et al., 1994;
243 Vairavamurthy, 1998). At Demerara Rise and Tarfaya Basin, the speciation of OS is
244 remarkably consistent before, during, and after the OAE-2 C-isotope excursion (Fig. 5),
245 contrasting the variation observed in the Pont d'Issole profile ((Raven et al., 2018); Fig. 5).
246 Additionally, as summarized in Table 1, the redox speciation of S-rich OM (S:C $\geq$ 3%) is

247 quite comparable at all four sites, with over half of OS present as alkyl sulfides and
248 substantial amounts of disulfides and sulfonates. There are subtle, yet robust, site-to-site
249 differences in OS speciation, with Demerara Rise OM richer in disulfides and leaner in
250 aromatic S forms than OM from Cismon, Tarfaya Basin, and Pont d'Issole shales. In less
251 strongly sulfurized samples from Pont d'Issole, the relative proportions of oxidized OS
252 forms – sulfonates and sulfate esters – are generally higher at the expense of alkyl sulfides
253 (Raven et al., 2018).
254
255 **Discussion**
256
257 **1. Organic S:C and local redox state**
258

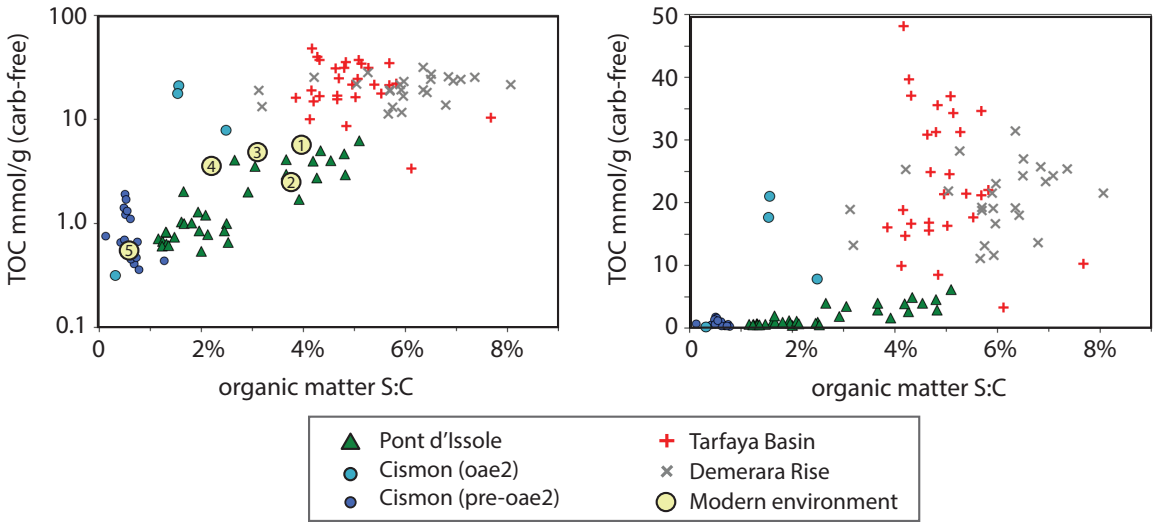

259

260 **Fig. 6 Global relationship between sulfurization intensity and TOC preservation.**
261 Relationships between the intensity of sulfurization (molar S:C ratio) and TOC
262 concentrations (mmol/g on a carbonate-free basis) are shown on log (left) and linear (right)

scales; for versions of these plots on a whole-rock basis, see Supplementary Figure 1. Circled numbers on left panel refer to published values from modern environments: (1) Cariaco Basin sediments (Werne et al., 2003); (2) the Peru Margin, (Eglinton et al., 1994); (3) the Namibian Margin, (Dale et al., 2009); (4) Santa Barbara Basin sediments, (Raven et al., 2016b); and (5) Gulf of Lion sediments (Supplementary Table 1).

Results from Cismon, Tarfaya Basin, and Demerara Rise extend the relationship between OM S:C ratio and abundance that was seen in Pont d'Issole (Raven et al., 2018), with samples ranging from OM–poor limestones to shales composed almost entirely of OM and carbonate (Figure 6). In addition to providing an indicator of the relative intensity of sulfurization reactions, the S:C ratio of OM can be used to infer the rate(s) and location of sulfurization (e.g., in particles sinking through the water column, at the sediment-water interface, or within the sediments). Elevated OM S:C ratios require organic substrates with a high density of functional groups available to react with (poly)sulfide; we refer to these groups as functionally 'sulfurizable moieties,' recognizing that certain moieties may be conditionally sulfurizable, contingent on the chemical and physical properties of the environment (Blair and Aller, 2012). Still, we broadly expect the highest concentrations of sulfurizable moieties in surface water, where fresh marine OM is relatively rich in sulfurizable aldehydes, alcohols, and conjugated double bonds (Amrani and Aizenshtat, 2004). The concentration of these moieties in particulate OM will decrease with depth as microbial heterotrophs degrade and consume oxygen- and energy-rich components of the milieu like sugars and proteins (Hedges et al., 1999).

286 Figure 6 illustrates how the relationship between the S:C ratio and concentration of OM
287 for the four compiled OAE-2 sites compares with published data from modern
288 environments with different redox conditions. Bottom waters from Cariaco Basin (labeled
289 '1') are sulfidic below ~250 m water depth (Werne et al., 2003); bottom waters from the
290 Peru ('2') and Namibian ('3') Margins are O_2-depleted but rarely sulfidic, with sulfidic
291 sediments (Dale et al., 2009; Eglinton et al., 1994); bottom waters in Santa Barbara Basin
292 ('4') are intermittently oxic, with sulfidic sediments; and both the bottom water and
293 shallow sediments in the Gulf of Lion sediments ('5') are oxic. Among these modern sites,
294 S:C ratios and OM concentrations are highest in sediments from the sulfidic Cariaco Basin
295 and lowest in sediments from the oxic Gulf of Lion. Sites with varying degrees of bottom
296 water O_2 depletion fall in between these end members, overlapping with Pont d'Issole
297 shales that similarly imply a chemocline near the sediment-water interface (Raven et al.,
298 2018). Of course, each of these sites is also affected by unique chemical and physical
299 characteristics of the environment. For example, high sedimentation rates are observed on
300 the Peru Margin due to the weathering of the Andes, which presumably dilutes TOC
301 concentrations relative to sites with more moderate sedimentation rates (Fig. 6). Despite
302 this caveat, these modern sites conform to a trend toward higher S:C ratios and higher OM
303 concentrations associated with increasingly O_2-limited environments.
304
305 The S:C ratios and TOC concentrations in modern sites overlap with the range of data from
306 Pont d'Issole and Cismon. At Pont d'Issole, variations in OM S:C ratio and OM
307 concentration correspond with changes in lithology and appear to record movement of the
308 chemocline between diffusively restricted sediments and the deeper water column (Raven

et al., 2018). In this interpretation, OM S:C ratios near 5% derive from rapid OM sulfurization reactions in the water column or near the sediment-water interface, where OM contains at least this concentration of functionally sulfurizable moieties, while during more oxic periods, sulfurization in sediments affects older OM (≥10s of years) with a lower concentration of sulfurizable moieties and yields OM S:C ratios closer to 2%. The redox speciation of OS from these purportedly oxic periods, as seen by XAS, is variable and distinct from OS in strongly sulfurized materials. In contrast, the distribution of OS redox states in strongly sulfurized OM is remarkably consistent within and among sites (Fig. 5). XAS results thus indicate that lower S:C ratios in some Pont d'Issole samples do not reflect simple dilution with a non-sulfurizable OM pool; instead, they indicate that sulfurization reactions involved a different suite of sulfurizable organic precursors, a different sulfur reactant (sulfide vs. polysulfide), or both.

Like at Pont d'Issole, OM-rich black shales from Cismon have previously been linked with bottom water anoxia based on sedimentological and bulk geochemical observations (Bellanca et al., 1996b). Cismon black shales have moderate S:C ratios (1.5–2.5%) but relatively high TOC concentrations compared with the other sites in Fig. 6, a potential effect of low sedimentation rates. On the other end of the spectrum, low-TOC limestones from Cismon are rich in benthic foraminifera, indicating generally oxic deposition. These sediments are comparable with low-TOC limestones from Pont d'Issole and modern oxic sediments from the Gulf of Lion, with typical S:C ratios of ≤1% (Fig. 6).

Southern proto–North Atlantic OAE-2 samples extend the trend in Figure 6 toward even greater OM concentrations and S:C ratios than those associated with bottom water anoxia at Cismon, Pont d'Issole, and modern sites. We lack modern analogues for these remarkable hotspots of organic C burial, which had an outsized role in driving changes in the OAE-2 C and S cycles (Sinninghe Damsté et al., 1998; Kolonic et al., 2005). At both Demerara Rise and Tarfaya Basin, there is abundant evidence for water column euxinia and at least intermittant photic zone anoxia. Finely laminated sediments from Demerara Rise (Erbacher et al., 2005) contain only occasional benthic foraminifera (Friedrich et al., 2006), iron speciation documents local sulfidic conditions (Owens et al., 2016), and trace metals also suggest reducing local conditions (Hetzel et al., 2009) that expand globally during the event (Owens et al., 2016). At Tarfaya, an anoxic and commonly sulfidic water column is evidenced by iron speciation, organic petrography, and the presence of biomarkers for phototrophic sulfide oxidizing bacteria (in nearby core S13, (Kuypers et al., 2002; Poulton et al., 2015). Still, there is also evidence for periodic, short-lived intervals of less strongly reducing conditions (Poulton et al., 2015), potentially contributing to slightly lower OM S:C ratios at this site than at Demerara. In general, however, reducing conditions at both southern proto–North Atlantic sites could have facilitated rapid, extensive sulfurization of a large pool of fresh OM in sinking particles with a high concentration of functionally sulfurizable moieties (Sinninghe Damsté et al., 1998). We emphasize that, in contrast with prior work, our conceptual model invokes near–instantaneous reactions between OM with some concentration of sulfurizable moieties and polysulfide, wherever sulfide and oxidants are first available in the environment. Polysulfide 'availability' for sulfurization will depend on microbial sulfate reduction rates,

354 oxidant availability, and competition with Fe; importantly, however, it does not necessarily
355 imply measurable free sulfide in the ('bulk') water column.
356
357 We can also compare these OAE-2 data with the results of laboratory experiments utilizing
358 algal biomass or model compounds. In the presence of excess polysulfides, lipids and
359 carbohydrates sulfurize to form macromolecular material in which characteristic
360 components have S:C ratios around 2–3% (Gelin et al., 1998) and ~6.7% (van Dongen et
361 al., 2003), respectively. For dissolved organic matter, bulk molar S:C ratios can apparently
362 be much higher, reaching as much as 15% in recent experiments (Pohlabeln et al., 2017).
363 Still, the average S:C ratios of (bulk, particulate) OM from Tarfaya (5.0%), Demerara
364 (5.9%), and Cismon shales (5.0%) indicate that the OM sulfurizing in these environments
365 had a concentration of sulfurizable moieties similar to the constituents of fresh,
366 carbohydrate–rich algal biomass. Experimental data thus lend credence to the hypothesis
367 that rapid, likely particle-hosted, sulfurization drove OM preservation in the water columns
368 of both Tarfaya Basin and Demerara Rise.
369
370 The relationship between S:C ratio, OM preservation, and local redox structure therefore
371 appears to be generalizable for marine environments, albeit with the important caveat that
372 concentration data are affected by local sedimentation rate. The observation that OM
373 sulfurization is an apparently major control on OM burial in diverse redox settings invites
374 parameterization and application of this trend to models of carbon cycling on local to global
375 scales and throughout the geologic record.
376

2. Interpreting organic matter and pyrite $\delta^{34}S$ records

To first order, the sulfur isotope compositions of pyrite and organic S reflect the $\delta^{34}S$ value of sulfide and/or polysulfide in the environment where that solid phase formed, with OM commonly ~5–10‰ more ^{34}S-enriched than coexisting pyrite (Anderson and Pratt, 1995). Accordingly, S–isotope ratios – of both pyrite and OM – provide potentially powerful archives of information about the availability and distribution of sulfide in the environment. Several primary factors affect the integrated (poly)sulfide $\delta^{34}S$ recorded in pyrite and OM, including (1) the $\delta^{34}S$ value of the sulfate used in microbial sulfate reduction (MSR; (Fike and Grotzinger, 2008); (2) the fractionation factor associated with MSR (ε_{MSR}, (Kaplan and Rittenberg, 1964)); (3) the position of the chemocline relative to diffusively 'closed' sediments (Jorgensen, 1979) and (4) the concentration of sulfate and resulting depth of sulfate depletion (Adams et al., 2010). Importantly, all of these processes impact the distribution and/or $\delta^{34}S$ value of (poly)sulfide in the environment and should therefore impact the S-isotope composition of both pyrite and OM, generating roughly parallel $\delta^{34}S$ profiles. If pyrite and OM $\delta^{34}S$ profiles are not parallel, then we need to invoke processes that affect these sinks differently.

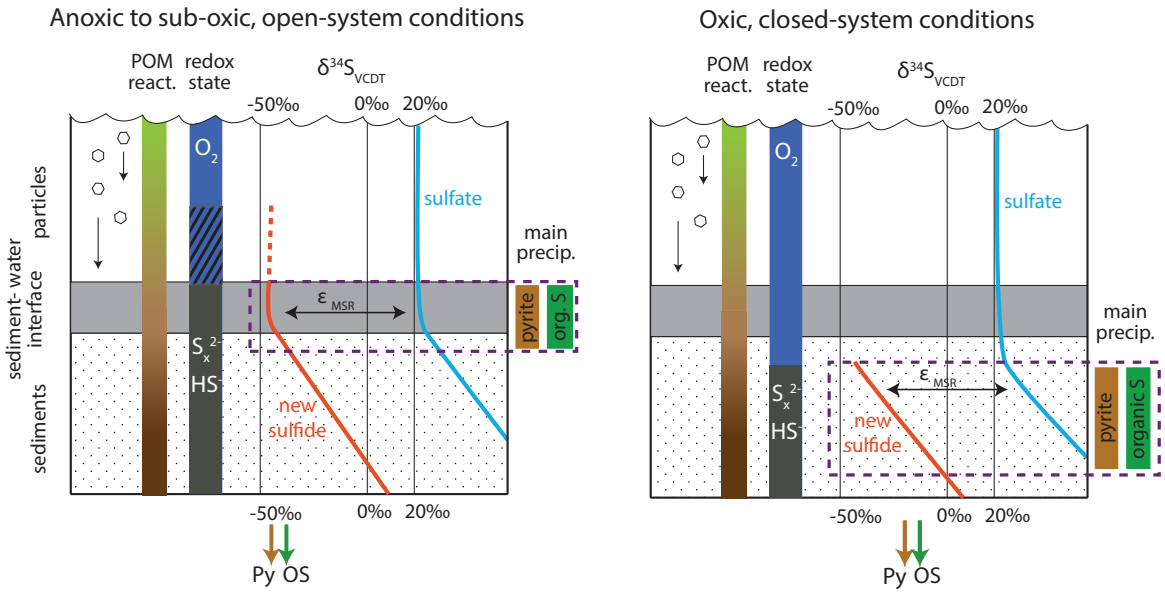

Fig. 7: Model for organic S and pyrite formation at Pont d'Issole and Cismon. The color scale labeled "POM react." represents a generalized decline in the reactivity of particulate OM with age since export from the photic zone. At left, the dashed red line and hatched redox state depict differences between sub-oxic and anoxic conditions. Under anoxic conditions, the zone of precipitation for pyrite and organic S would move upward with the chemocline. Diagram is not to scale.

At Pont d'Issole, OM and pyrite $\delta^{34}S$ profiles move in near–parallel between the TOC-rich and TOC-lean layers associated with OAE-2 (Fig. 2). In a previous study, we attributed these $\delta^{34}S$ trends in OM to changes in the position of the chemocline in the paleo-environment, meaning that MSR moved between environments that were diffusively open or closed systems with respect to sulfate, shown schematically in Fig. 7. Under conditions where O_2 concentrations are drawn down to zero at roughly the sediment-water interface (which we call 'sub-oxic' in Fig. 7), MSR in the shallowest sediments can access the open-

411 ocean pool of seawater sulfate with an unfractionated $\delta^{34}S$ value, and the resulting strongly
412 ^{34}S-depleted sulfide from MSR is recorded in both pyrite and OM. Under more 'oxic'
413 conditions, O_2 penetrates deeper in the sediments and microbial sulfate reduction occurs in
414 a diffusively sulfate–limited environment. As available sulfate is consumed with some
415 fractionation (ε_{MSR}), residual sulfate in porewater becomes enriched in ^{34}S, and the organic
416 and inorganic sulfur pools that precipitate within such a (partially) closed system have
417 higher integrated $\delta^{34}S$ values than those formed in open systems. At Pont d'Issole, S–
418 isotope evidence for closed-system MSR is also associated with smaller amounts of
419 preserved OM with a lower S:C ratio.
420
421 The S-isotope data for OS and pyrite from Cismon shales are consistent with the open–vs–
422 closed system dynamics indicated at Pont d'Issole. Both phases are strongly ^{34}S-depleted
423 during the OAE C-isotope excursion, indicating generally open-system pyrite and OS
424 formation. These low $\delta^{34}S$ values are similar to S-isotope data observed in sediments from
425 modern sulfidic basins, which have been attributed to open-system formation (Lyons et al.,
426 2003). As noted by the dashed vertical red line in Fig. 7, the critical sulfidic environment(s)
427 hosting these reactions could be very shallow sediments and/or particles sinking through
428 the water column.
429

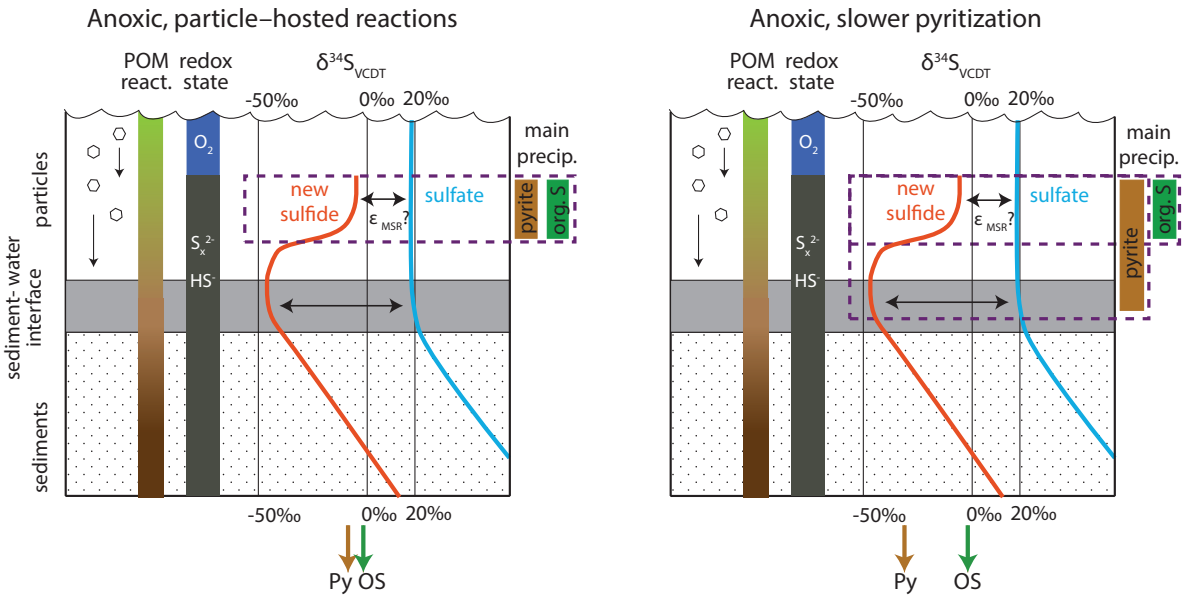

Fig. 8 Proposed model for OAE-2 $\delta^{34}S$ records at Tarfaya and Demerara. Left panel shows hypothesized conditions ≥190,000 yrs before the onset of OAE-2. Right panel shows a scenario for explaining pyrite and OM $\delta^{34}S$ values during the early part of the OAE-2 C-isotope excursion. The color scale labeled "POM react." represents a generalized decline in the reactivity of particulate OM with age since export from the photic zone. Diagram is not to scale.

In contrast, different processes impact $\delta^{34}S$ patterns at Tarfaya Basin and Demerara Rise. A wealth of data supports the idea that the Tarfaya Basin and Demerara Rise water columns were typically euxinic before and after OAE-2, which would imply open-system S cycling that leads to ^{34}S-depleted pyrite and OM. Yet, $\delta^{34}S$ values of pyrite and OM from both of these sites are near –5‰ at these times, much more ^{34}S-enriched than samples from other sites with open-system MSR. To reconcile these observations, we propose that the $\delta^{34}S$ values recorded in plentiful OM at Tarfaya Basin and Demerara Rise do reflect the S-

445 isotope composition of sulfide in sinking particles, and that this sulfide was relatively ^{34}S-
446 enriched (Fig. 8). Similarly, there is limited evidence for the existence of transiently ^{34}S-
447 enriched sulfide in particles from Cariaco Basin, despite deep basin sulfide δ^{34}S values that
448 are consistently near –30‰ (Li et al., 2010). During a period of peak productivity and
449 apparent sulfurization, the elemental S in sinking particles had δ^{34}S values between –5.9
450 and 18.9‰ (Raven et al., 2016a), a δ^{34}S offset from seawater sulfate of only 2 to 27‰. The
451 dramatic enrichment inferred for particle sulfide δ^{34}S values at Tarfaya Basin and
452 Demerara Rise (Fig. 8) contrasts with the slight (~5‰) enrichments frequently observed in
453 the uppermost portion of modern sulfidic water columns (Lyons et al., 2003), which are
454 attributed to oxidative S-cycling microorganisms and/or abiotic sulfide oxidation. Thus,
455 the ^{34}S-enriched patterns in OM and pyrite in OM-rich sediments may capture the signature
456 of MSR occurring rapidly in sinking particles.
457
458 The large fluxes of fresh OM that reached O_2-limited parts of the environment in both
459 Tarfaya Basin and Demerara Rise make these sites likely candidates for the operation of
460 rapid, substrate-replete MSR, which could lead to relatively ^{34}S-enriched sulfide in
461 particles via smaller fractionations during sulfate reduction, sulfate drawdown within
462 diffusively limited microenvironments, or both. The fractionation factor associated with
463 MSR (ε_{MSR}) is highly variable and depends broadly on the rate of MSR (Kaplan and
464 Rittenberg, 1964). Although most marine systems have apparent fractionation factors
465 closer to the equilibrium fractionation between sulfate and sulfide of 72‰, low ε_{MSR} values
466 (<25‰) are associated with high rates of cell-specific MSR, on the order of >25 fmol
467 H_2S/cell/day (Wenk et al., 2017), observed for sulfate reducers in laboratory settings with

plentiful carbon substrates and nutrients. These "small" S-isotope fractionations are consistent with the 20–30‰ difference between seawater sulfate (at ~19‰) and apparent particle-hosted sulfide observed at Tarfaya Basin and Demerara Rise. Alternatively or in addition to changes in ε_{MSR}, if particles are sufficiently large (>> 1 mm), it is possible for sulfate to become diffusively limited within particle microenvironments (Louca and Crowe, 2017). Very high rates of MSR could therefore drive the remaining sulfate pool within microenvironments toward higher $\delta^{34}S$ values and contribute to relatively ^{34}S-enriched sulfide.

The alternative explanation for our results attributes the relatively ^{34}S-enriched composition of pyrite and OM at Tarfaya and Demerara prior to the onset of the OAE to their formation from sediment porewater. Importantly, it also requires that these phases form semi-continuously during burial to the depths at which sulfate is nearly fully drawn down, in order to integrate to bulk compositions near –5‰. Barring extreme sedimentation events, this implies maximum OM sulfurization rates on the timescales of at least tens to hundreds of years – sufficient to accumulate a diffusively limiting layer – not the days to weeks observed in Cariaco particles and laboratory experiments. Additionally, this explanation for Tarfaya and Demerara $\delta^{34}S$ patterns is difficult to reconcile with the S:C ratio of OM. For OM to incorporate up to 6 mol% S gradually over at least years of aging, that OM must have retained a high density of sulfurizable moieties that were somehow also effectively inaccessible to heterotrophs. Theoretically, this could result from enhanced preservation mechanisms other than sulfurization, notably physical protection by association with clays or other mineral surfaces (Hedges and Keil, 1995). Still, the sheer

491 abundance of OM in Tarfaya and Demerara sediments would overwhelm available clays,
492 and it is difficult to envision a mechanism to sulfurize OM after many years of effective
493 physical protection. We therefore consider a purely closed-system sedimentary origin for
494 the moderately ^{34}S-enriched OM and pyrite at Tarfaya and Demerara improbable.
495
496 Similar to OM throughout the section, pyrite in the lowest part of the section at both
497 Tarfaya Basin and Demerara Rise has relatively high $\delta^{34}S$ values. Under these pre-OAE-2
498 conditions, the offset between pyrite and OM $\delta^{34}S$ values is only 5–10‰, similar to the
499 offset observed in other environments that are thought to host open-system concurrent
500 pyritization and OM sulfurization (Cariaco Basin, Cismon). Starting significantly before
501 the onset of OAE-2, pyrite $\delta^{34}S$ begins to move independently of OM $\delta^{34}S$, increasing
502 $\Delta\delta^{34}S_{OS\text{-}py}$ values. Little-to-no concurrent shift is seen in the OM $\delta^{34}S$ record, and OM has
503 a consistent S redox composition (as assessed by XAS, Fig. 5) throughout the section.
504 Therefore, the shift in pyrite $\delta^{34}S$ values is not the result of changing sulfide distribution or
505 ε_{MSR} in the environment. Instead, this independent variability is caused by a process that
506 impacts the kinetics of one sulfide sink relative to the other. In the case of pyrite at the
507 onset of OAE-2 at Tarfaya and Demerara Rise, the observed shift indicates that the zone
508 of pyrite formation expanded into deeper portions of the water column and/or sediment,
509 integrating more ^{34}S-depleted sulfide generated from MSR at more typical (slow)
510 environmental rates (Fig. 8).
511

512 3. Global pyrite $\delta^{34}S$ patterns and OAE-2 implications

513

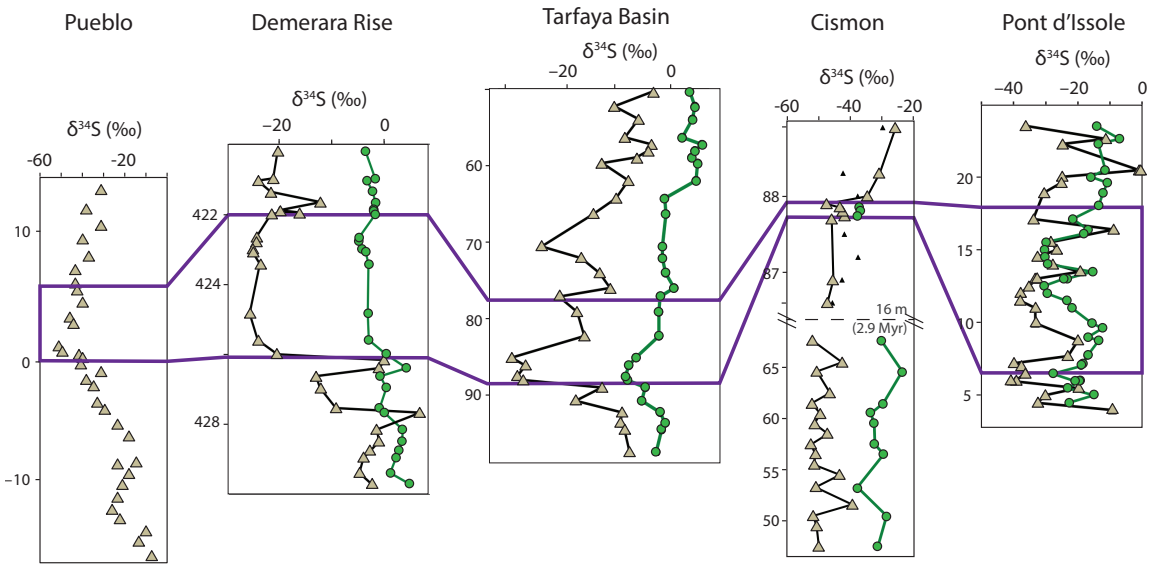

Fig. 9 Summary of $\delta^{34}S$ records across OAE-2. Green circles show OM $\delta^{34}S$ values and brown triangles show pyrite $\delta^{34}S$ values. Pueblo data is from (Adams et al., 2010). The gap in the Cismon y-axis represents 16 m of OM-lean carbonates (~2.9 Myr), and small black triangles are previously published data from (Gomes et al., 2016). The C-isotope excursion, representing an estimated 500 kyr of accumulation, is outlined in purple. Pyrites from Demerara Rise, Tarfaya Basin, and Pueblo all become more ^{34}S-depleted leading up to the onset of OAE-2.

The decrease in pyrite $\delta^{34}S$ values prior to the onset of OAE-2 appears to be a widespread phenomenon, with remarkably similar profiles from Demerara Rise, Tarfaya Basin, and the Western Interior Seaway (Pueblo (Adams et al., 2010), Fig. 9). Because the ~20‰ negative $\delta^{34}S$ shift in pyrite at Tarfaya and Demerara is not observed in the $\delta^{34}S$ profile of OM, it is not likely to primarily reflect changes in the spatial distribution or $\delta^{34}S$ of dissolved sulfide in the environment. Instead, we propose that pyrite $\delta^{34}S$ patterns record

529 changes in marine iron cycling across OAE-2, which impacted the kinetics of pyrite
530 precipitation and extended the zone of pyrite precipitation deeper in the sedimentary
531 profile.
532
533 The iron available for pyritization in marine environments is sourced from a mixture of
534 detrital iron from the continents, hydrothermal iron from spreading ridges, and remobilized
535 iron from biogeochemical cycling in shelf sediments. Most sediments from the southern
536 proto–North Atlantic during OAE-2 have elevated Fe_T/Al ratios (>0.5, the crustal average
537 value) and near–zero $\delta^{56}Fe$ compositions, suggesting that a significant component of the
538 iron delivered to these sites was from hydrothermal sources (Owens et al., 2012). The
539 processes that facilitate the transport of hydrothermally-sourced iron remain subjects of
540 active research, but appear to involve stabilization of Fe^{3+} in colloidal or nanoparticulate
541 phases (Fitzsimmons et al., 2017). Hydrothermal iron that encounters dissolved sulfide can
542 precipitate as an Fe-sulfide and be trapped in place as pyrite, restricting the amount of iron
543 that can be transported through euxinic basins to distal sites. In contrast, iron is highly
544 mobile in anoxic but non-sulfidic seawater. The delivery of iron to Demerara Rise and
545 Tarfaya Basin was therefore likely sensitive to the redox state of nearby environments, and
546 hydrothermal iron delivery could have been significantly curtailed by nearby euxinia.
547
548 In addition to impacting the total flux of iron transported throughout the basin, expanding
549 anoxia is likely to affect its mineralogy. The source of Fe for pyritization is commonly
550 presumed to be dissolved Fe^{2+}, which can be released from Fe^{III}-bearing minerals by
551 reduction either abiotically with bisulfide (Canfield, 1989) or biotically by Fe-reducing

552 microorganisms. The rates of both types of iron reduction vary depending on the
553 mineralogy and specific surface area of the Fe^{III} involved: poorly crystalline oxyhydroxides
554 like ferrihydrite and lepidocrocite are reduced within hours to days, while crystalline oxides
555 and oxyhydroxides like goethite and hematite are reduced more slowly, and Fe-bearing
556 silicates can persist for millennia (Raiswell et al., 2018). Where concentrations of Fe^{2+} and
557 sulfide in solution are sufficiently high, pyrite precipitation is generally thought to proceed
558 via precipitation of an iron monosulfide intermediate that subsequently converts to pyrite.
559 Intriguingly, (Wan et al., 2017) recently described a second category of pyritization
560 mechanism with the potential to drive pyrite formation where Fe^{III}–oxide surfaces are
561 plentiful and vastly exceed the available HS^-. Under these conditions, ferric hydroxide
562 surfaces can mediate the rapid nucleation of pyrite via the formation of $>Fe^{II}S_2^-$, making
563 redox interfaces and sinking particles with high Fe^{III}:HS^- ratios potential hotspots for
564 surface-mediated pyritization of ferric hydroxides. Ferric hydroxides from any source
565 (hydrothermal, detrital, or remobilized) would have been less likely to reach already-
566 euxinic sites like Demerara Rise and Tarfaya Basin as regional euxinia expanded, raising
567 the possibility that the negative shift in pyrite S-isotopes reflects a reduction in the
568 significance of this pyritization mechanism. Changing regional redox could also impact the
569 mineralogy of remobilized Fe more broadly by changing the rates and/or environmental
570 conditions of (oxy)hydroxide formation during repetitive redox cycling, generating a
571 different suite of Fe^{III} minerals that re-release Fe^{2+} into the depositional environment at
572 diverse rates. The bulk pyrite $\delta^{34}S$ records we present here reflect the integrated pool of
573 pyrite derived from precipitation on multiple timescales of Fe^{III}–mineral (re-)reduction as
574 well as potentially from ferric hydroxide surface–mediated reactions. Separating these

575 various contributors to bulk pyrite records will be essential to understand how expanding
576 regional anoxia and euxinia impacted the abundance and mineralogy of iron sources and,
577 by extension, the kinetics of pyritization.
578
579 Trace metal concentrations and thallium isotopes from Demerara Rise provide evidence
580 for the expansion of regional to more global anoxia prior to the onset of the OAE-2 C-
581 isotope excursion (Ostrander et al., 2017; Owens et al., 2016). Like iron, the redox-
582 sensitive elements Zn, V, and Mo are readily sequestered in anoxic and/or sulfidic
583 sediments, and this process is thought to be responsible for their apparent removal from
584 seawater prior to OAE-2 (Owens et al., 2016). Using an extrapolation of the estimated
585 OAE-2 linear sedimentation rate (0.8 cm/kyr) to 427.5 m, pyrite $\delta^{34}S$ values at Demerara
586 begin to decrease ~190 kyr before the onset of OAE-2. This depth corresponds to the initial
587 drop in concentrations of Zn in this core, a sensitive indicator of anoxic conditions with a
588 short residence time (~11 kyr, (Little et al., 2014)). The decrease in pyrite $\delta^{34}S$ values
589 culminates at the onset of the OAE, in sediments evidencing drawdown of even sulfide-
590 sensitive Mo, indicating prevalent sulfidic environments (Owens et al., 2016). The gradual
591 pre-OAE pyrite $\delta^{34}S$ shift at Demerara thus corresponds to a period of intensification of
592 regional to global anoxia prior to the OAE and an expansion of sulfidic conditions globally
593 (Owens et al., 2013).
594
595 Changes in the delivery of iron to sites in the southern proto–North Atlantic could have
596 generated the shift in pyrite $\delta^{34}S$ that we observe by slowing the kinetics of pyrite
597 formation. For example, if the combination of expanding euxinia and volcanic activity

598 caused the main source of Fe at these sites to switch from more hydrothermally sourced,
599 organic–complexed Fe^{III} to detrital or volcanic crystalline oxy-hydroxides, the rate of Fe^{2+}
600 release to solution in sinking marine particles could have dropped dramatically. The
601 conceptual model put forth in Fig. 7 predicts that this scenario would yield more ^{34}S-
602 depleted pyrite overall. Importantly, this could occur while the total quantity of pyrite
603 eventually buried remained nearly constant.
604
605 At Pueblo and Tarfaya Basin, the onset of the shift toward more ^{34}S-depleted pyrite is
606 staggered relative to Demerara Rise (Fig. 9). Using published interpolated Ar-Ar ages from
607 ammonite biozones, pyrite $\delta^{34}S$ values at Pueblo drop in two stages at ~400 kyr and ~200
608 kyr before the onset of OAE-2 (Adams et al., 2010). At Tarfaya Basin, if we extrapolate
609 estimated OAE-2 accumulation rates (3.3 cm/kyr) similar to Demerara, then the pyrite $\delta^{34}S$
610 shift occurs ~82 kyr before the OAE. Osmium, strontium, and other geochemical proxies
611 indicate regional heterogeneity in hydrothermal activity in different ocean basins at this
612 time (du Vivier et al., 2014), which would also impact hydrothermal iron fluxes (Owens et
613 al., 2012). Importantly, the Western Interior Seaway has a different redox structure leading
614 up to OAE-2 than the rest of the proto-North Atlantic and Tethys, which likely leads to
615 differences in the history of iron cycling among these sites.
616
617 Records from OAE-2 exemplify how the timing and location of pyritization can be affected
618 by changes in iron biogeochemistry in addition to changes in sulfur cycling. They also
619 suggest that organic S should be incorporated into future models for the S cycle for OAEs.
620 For example, because organic S is more typically more ^{34}S-enriched than pyrite, previous

621 estimates for the extent of euxinia during OAE-2 based on S-isotope mass balance (e.g.,
622 Owens et al., 2013) may be conservative. OM sulfurization could have been important
623 factor for driving high organic carbon mass accumulation rates even for localities with low
624 total organic carbon (Owens et al., 2018), supporting massive global OC burial. By
625 investigating the S-isotope behavior of both pyrite and OM, we can begin to take full
626 advantage of these complex and powerful archives.
627
628 **Conclusions**
629 In sedimentary sections spanning OAE-2, the S-isotope compositions of pyrite were
630 impacted by the confluence of local redox structure, the fractionation associated with
631 microbial sulfate reduction (ε_{MSR}), and the speciation of Fe in the environment, while the
632 S-isotope compositions of OM appear to predominantly reflect changes in local redox
633 structure and/or ε_{MSR}. Accordingly, paired OM and pyrite $\delta^{34}S$ profiles make it possible to
634 disentangle the effects of chemocline position, sulfate reduction rate, and regional-to-
635 global geochemical perturbations on S-isotopes in the rock record.
636
637 Particle-hosted OM sulfurization may be a primary control on OM preservation during
638 periods of widespread OM burial. Explicit consideration of rapid OM sulfurization in O_2-
639 limited environments thus has the potential to improve models of organic C preservation
640 and remineralization in both modern and ancient systems. Additionally, in the several
641 hundred thousand years leading up to the onset of OAE-2, paired pyrite and OM $\delta^{34}S$
642 records indicate a globally widespread change in the timing of pyrite formation relative to
643 OM sulfurization. The regional expansion of euxinic conditions and changes in volcanic

644 activity may have contributed to changes in the speciation of iron available for pyritization
645 and thus to the relatively slow formation of relatively ^{34}S-depleted pyrite during the OAE.
646 This change in global Fe-cycling could not be identified from pyrite $\delta^{34}S$ profiles alone,
647 underscoring the value and untapped potential of paired pyrite – OM S-isotope records for
648 exploring geologic archives.
649
650
651 **Acknowledgements**
652 We are grateful for financial support to M.R.R. from the Agouron Institute (Geobiology
653 Post-doctoral fellowship) and to Itay Halevy (Weizmann Institute, Israel), Matt Hurtgen,
654 and Brad Sageman (Northwestern University, USA) for valuable discussions. Melanie
655 Suess, Jen Houghton, and Stephanie Moore provided technical support for analyses at
656 Washington University in St. Louis. Tarfaya and Demerara samples were obtained via
657 Wolfgang Kuhnt (Kiel University) and IODP, respectively. This work was enhanced by
658 XAS analyses at the Stanford Synchrotron Radiation Laboratory under Rapid Access User
659 Proposal 49705, as well as the efforts of SSRL staff. Use of the Stanford Synchrotron
660 Radiation Lightsource, SLAC National Accelerator Laboratory, is supported by the U.S.
661 Department of Energy, Office of Science, Office of Basic Energy Sciences under Contract
662 No. DE-AC02-76SF00515.
663
664 **Supplemental Information:**
665 Fig. S1: whole-rock basis version of Fig. 6
666 Table S1: Gulf of Lion average composition

667 Table S2: Compiled geochemical results

668 Table S3: Compiled XAS results

669

References

Adams, D.D., Hurtgen, M.T., Sageman, B.B., 2010. Volcanic triggering of a biogeochemical cascade during Oceanic Anoxic Event 2 3, 201–204.

Amrani, A., Aizenshtat, Z., 2004. Mechanisms of sulfur introduction chemically controlled: δ34S imprint. Organic Geochemistry 35, 1319–1336. doi:10.1016/j.orggeochem.2004.06.019

Anderson, T.F., Pratt, L.M., 1995. Isotopic evidence for the origin of organic sulfur and elemental sulfur in marine sediments 612, 378–396.

Bellanca, A., Claps, M., Erba, E., Masetti, D., Neri, R., 1996a. Orbitally induced limestone/marlstone rhythms in the Albian—Cenomanian Cismon section (Venetian region, northern Italy): Sedimentology, calcareous and siliceous …. Palaeogeography 126, 227–260. doi:10.1016/S0031-0182(96)00041-7

Bellanca, A., Claps, M., Erba, E., Masetti, D., Neri, R., Premoli Silva, I., Venezia, F., 1996b. Orbitally induced limestone/marlstone rhythms in the Albian—Cenomanian Cismon section (Venetian region, northern Italy): Sedimentology, calcareous and siliceous plankton distribution, elemental and isotope geochemistry. Palaeogeography, Palaeoclimatology, Palaeoecology 126, 227–260. doi:10.1016/S0031-0182(96)00041-7

Blair, N.E., Aller, R.C., 2012. The Fate of Terrestrial Organic Carbon in the Marine Environment. Annu. Rev. Mar. Sci. 4, 401–423. doi:10.1146/annurev-marine-120709-142717

Boussafir, M., Gelin, F., Lallier-Verges, E., Derenne, S., Bertrand, P., Largeau, C., 1995. Electron microscopy and pyrolysis of kerogens from the Kimmeridge Clay Formation, UK: Source organisms, preservation processes, and origin of microcycles. Geochimica et Cosmochimica Acta 59, 3731–3747.

Canfield, D.E., 1989. Reactive iron in marine sediments. Chemical Geology 53, 619–632. doi:10.1016/0016-7037(89)90005-7

Canfield, D.E., Raiswell, R., Westrich, J.T., Reaves, C.M., 1986. The use of chromium reduction in the analysis of reduced inorganic sulfur in sediments and shales. Chemical Geology.

Dale, A.W., Bruchert, V., Alperin, M., Regnier, P., 2009. An integrated sulfur isotope model for Namibian shelf sediments. Geochimica et Cosmochimica Acta 73, 1924–1944. doi:10.1016/j.gca.2008.12.015

Damsté, J., Letters, J.K.E.A.P.S., 1998, 1998. A euxinic southern North Atlantic Ocean during the Cenomanian/Turonian oceanic anoxic event. Chemical Geology 158, 165–173.

Eglinton, T.I., Irvine, J.E., Vairavamurth, Zhou, W., Manowitz, B., 1994. Formation and diagenesis of macromolecular organic sulfur in Peru margin sediments. Organic Geochemistry 22, 781–799.

Erbacher, J., Friedrich, O., Wilson, P.A., Birch, H., Mutterlose, J., 2005. Stable organic carbon isotope stratigraphy across Oceanic Anoxic Event 2 of Demerara Rise, western tropical Atlantic. Geochemistry Geophysics Geosystems 6, 714–9. doi:10.1029/2004GC000850

Fike, D.A., Grotzinger, J.P., 2008. A paired sulfate–pyrite δ34S approach to understanding the evolution of the Ediacaran–Cambrian sulfur cycle. Geochimica et Cosmochimica Acta 72, 2636–2648. doi:10.1016/j.gca.2008.03.021

Fitzsimmons, J.N., John, S.G., Marsay, C.M., Hoffman, C.L., Nicholas, S.L., Toner, B.M., German, C.R., Sherrell, R.M., 2017. Iron persistence in a distal hydrothermal plume supported by dissolved–particulate exchange. Nature Geosci 10, 195–201. doi:10.1038/ngeo2900

Gambacorta, G., Jenkyns, H.C., Russo, F., Tsikos, H., Wilson, P.A., Faucher, G., Erba, E., 2015. Carbon- and oxygen-isotope records of mid-Cretaceous Tethyan pelagic sequences from the Umbria – Marche and Belluno Basins (Italy). Newsl. Stratigr. 48, 299–323. doi:10.1127/nos/2015/0066

Gelin, F., Kok, M.D., De Leeuw, J.W., Damsté, J.S.S., 1998. Laboratory sulfurisation of the marine microalga Nannochloropsis salina. Organic Geochemistry 29, 1837–1848.

Gomes, M.L., Hurtgen, M.T., Sageman, B.B., 2016. Biogeochemical sulfur cycling during Cretaceous oceanic anoxic events: A comparison of OAE1a and OAE2. Paleoceanography 1–19. doi:10.1002/(ISSN)1944-9186

Hedges, J.I., Hu, F.S., Devol, A.H., Hartnett, H.E., Tsamakis, E., Keil, R.G., 1999. Sedimentary organic matter preservation; a test for selective degradation under oxic conditions. American Journal of Science 299, 529–555.

Hetzel, A., Böttcher, M.E., Wortmann, U.G., Brumsack, H.-J., 2009. Paleo-redox conditions during OAE 2 reflected in Demerara Rise sediment geochemistry (ODP Leg 207). Palaeogeography, Palaeoclimatology, Palaeoecology 273, 302–328. doi:10.1016/j.palaeo.2008.11.005

Jarvis, I., Lignum, J.S., Gröcke, D.R., Jenkyns, H.C., 2011. Black shale deposition, atmospheric CO2 drawdown, and cooling during the Cenomanian-Turonian Oceanic Anoxic Event. Paleoceanography 26. doi:10.1029/2010PA002081

Jorgensen, B.B., 1979. A theoretical model of the stable sulfur isotope distribution in marine sediments. Geochimica et Cosmochimica Acta 43, 363–374.

Kaplan, I.R., Rittenberg, S.C., 1964. Microbiological fractionation of sulphur isotopes. Journal of General Microbiology 34, 195–212.

Keller, G., Adatte, T., Berner, Z., Chellai, E.H., Stueben, D., 2008. Oceanic events and biotic effects of the Cenomanian-Turonian anoxic event, Tarfaya Basin, Morocco. Cretaceous Research 29, 976–994. doi:10.1016/j.cretres.2008.05.020

Kolonic, S., Damsté, J., Böttcher, M.E., Kuypers, M.M.M., Kuhnt, W., Scheeder, G., Wagner, T., beckmann, B., 2002. Geochemical characterization of Cenomanian/Turonian black shales from the Tarfaya Basin (SW Morocco). Journal

of Petroleum Geology 25, 325–350.

Kolonic, S., Wagner, T., Forster, A., Sinninghe Damsté, J.S., Walsworth-Bell, B., Erba, E., Turgeon, S., Brumsack, H.-J., Chellai, E.H., Tsikos, H., Kuhnt, W., Kuypers, M.M.M., 2005. Black shale deposition on the northwest African Shelf during the Cenomanian/Turonian oceanic anoxic event: Climate coupling and global organic carbon burial. Paleoceanography 20, n/a–n/a. doi:10.1029/2003PA000950

Kuypers, M.M.M., Pancost, R.D., Nijenhuis, I.A., Sinninghe Damsté, J.S., 2002. Enhanced productivity led to increased organic carbon burial in the euxinic North Atlantic basin during the late Cenomanian oceanic anoxic event. Paleoceanography 17, 3–1–3–13. doi:10.1029/2000PA000569

Li, X., Gilhooly, W.P., III, Zerkle, A.L., Lyons, T.W., Farquhar, J., Werne, J.P., Varela, R., Scranton, M.I., 2010. Stable sulfur isotopes in the water column of the Cariaco Basin. Geochimica et Cosmochimica Acta 74, 6764–6778. doi:10.1016/j.gca.2010.08.020

Little, S.H., Vance, D., Walker-Brown, C., Landing, W.M., 2014. The oceanic mass balance of copper and zinc isotopes, investigated by analysis of their inputs, and outputs to ferromanganese oxide sediments. Geochimica et Cosmochimica Acta 125, 673–693. doi:10.1016/j.gca.2013.07.046

Louca, S., Crowe, S.A., 2017. Microscale reservoir effects on microbial sulfur isotope fractionation. Geochimica et Cosmochimica Acta 203, 117–139. doi:10.1016/j.gca.2017.01.007

Lyons, T.W., Werne, J.P., Hollander, D.J., Murray, R.W., 2003. Contrasting sulfur geochemistry and Fe/Al and Mo/Al ratios across the last oxic-to-anoxic transition in the Cariaco Basin, Venezuela. Chemical Geology 195, 131–157. doi:10.1016/S0009-2541(02)00392-3

Ostrander, C.M., Owens, J.D., Nielsen, S.G., 2017. Constraining the rate of oceanic deoxygenation leading up to a Cretaceous Oceanic Anoxic Event (OAE-2: ~94 Ma). Science Advances 1–6.

Owens, J.D., Gill, B.C., Jenkyns, H.C., 2013. Sulfur isotopes track the global extent and dynamics of euxinia during Cretaceous Oceanic Anoxic Event 2, in:. Presented at the Proceedings of the …. doi:10.1073/pnas.1305304110/-/DCSupplemental

Owens, J.D., Lyons, T.W., Li, X., Macleod, K.G., 2012. Iron isotope and trace metal records of iron cycling in the proto North Atlantic during the Cenomanian Turonian oceanic anoxic event (OAE 2). Paleoceanography. doi:10.1029/2012PA002328

Owens, J.D., Lyons, T.W., Lowery, C.M., 2018. Quantifying the missing sink for global organic carbon burial during a Cretaceous oceanic anoxic event. Earth and Planetary Science Letters 499, 83–94. doi:10.1016/j.epsl.2018.07.021

Owens, J.D., Reinhard, C.T., Rohrssen, M., Love, G.D., Lyons, T.W., 2016. Empirical links between trace metal cycling and marine microbial ecology during a large perturbation to Earth's carbon cycle. Earth and Planetary Science Letters 449, 407–417. doi:10.1016/j.epsl.2016.05.046

790 Pohlabeln, A.M., Gomez-Saez, G.V., Noriega-Ortega, B.E., Dittmar, T., 2017.
791 Experimental Evidence for Abiotic Sulfurization of Marine Dissolved Organic
792 Matter. Front. Mar. Sci. 4, 265. doi:10.3389/fmars.2017.00364

793 Poulton, S.W., Henkel, S., März, C., Urquhart, H., Flögel, S., Kasten, S., Sinninghe
794 Damsté, J.S., Wagner, T., 2015. A continental-weathering control on orbitally driven
795 redox-nutrient cycling during Cretaceous Oceanic Anoxic Event 2. Geology 43, 963–
796 966. doi:10.1130/G36837.1

797 Raiswell, R., Hardisty, D.S., Lyons, T.W., Canfield, D.E., Owens, J.D., Planavsky, N.J.,
798 Poulton, S.W., Reinhard, C.T., 2018. The iron paleoredox proxies: A guide to the
799 pitfalls, problems and proper practice. American Journal of Science 318, 491–526.
800 doi:10.2475/05.2018.03

801 Raven, M.R., Fike, D.A., Gomes, M.L., Webb, S.M., Bradley, A.S., McClelland, H.-
802 L.O., 2018. Organic carbon burial during OAE2 driven by changes in the locus of
803 organic matter sulfurization. Nature Communications 9, 3409. doi:10.1038/s41467-
804 018-05943-6

805 Raven, M.R., Sessions, A.L., Adkins, J.F., Thunell, R.C., 2016a. Rapid organic matter
806 sulfurization in sinking particles from the Cariaco Basin water column. Geochimica
807 et Cosmochimica Acta 190, 175–190. doi:10.1016/j.gca.2016.06.030

808 Raven, M.R., Sessions, A.L., Fischer, W.W., Adkins, J.F., 2016b. Sedimentary pyrite δ
809 34 S differs from porewater sulfide in Santa Barbara Basin: Proposed role of organic
810 sulfur. Geochimica et Cosmochimica Acta 186, 120–134.
811 doi:10.1016/j.gca.2016.04.037

812 Sageman, B.B., Meyers, S.R., Arthur, M.A., 2006. Orbital time scale and new C-isotope
813 record for Cenomanian-Turonian boundary stratotype. Geology 34, 125–4.
814 doi:10.1130/G22074.1

815 Vairavamurthy, A., 1998. Using X-ray absorption to probe sulfur oxidation states in
816 complex molecules. Spectrochimica Acta Part A: Molecular and … 54, 2009–2017.
817 doi:10.1016/S1386-1425(98)00153-X

818 van Dongen, B.E., Schouten, S., Baas, M., Geenevasen, J.A.J., Sinninghe Damsté, J.S.,
819 2003. An experimental study of the low-temperature sulfurization of carbohydrates.
820 Organic Geochemistry 34, 1129–1144. doi:10.1016/S0146-6380(03)00060-3

821 Vivier, Du, A.D.C., Selby, D., Sageman, B.B., Jarvis, I., Gröcke, D.R., Voigt, S., 2014.
822 Marine 187Os/188Os isotope stratigraphy reveals the interaction of volcanism and
823 ocean circulation during Oceanic Anoxic Event 2. Earth and Planetary Science
824 Letters 389, 23–33. doi:10.1016/j.epsl.2013.12.024

825 Wan, M., Schröder, C., Peiffer, S., 2017. Fe (III): S (-II) Concentration Ratio Controls the
826 Pathway and the Kinetics of Pyrite Formation during Sulfidation of Ferric
827 Hydroxides. Geochimica et Cosmochimica Acta. doi:10.1016/j.gca.2017.08.036

828 Webb, S.M., 2005. SIXpack: a graphical user interface for XAS analysis using IFEFFIT.
829 Phys. Scr. 2005, 1011. doi:10.1238/Physica.Topical.115a01011

830 Wenk, C.B., Wing, B.A., Halevy, I., 2017. Electron carriers in microbial sulfate reduction
831 inferred from experimental and environmental sulfur isotope fractionations 1–13.
832 doi:10.1038/ismej.2017.185

833 Werne, J.P., Lyons, T.W., Hollander, D.J., Chemical, M.F., Sinninghe Damsté, J.S.,
834 2003. Reduced sulfur in euxinic sediments of the Cariaco Basin: sulfur isotope
835 constraints on organic sulfur formation. Chemical Geology 195, 159–179.
836 doi:10.1016/S0009-2541(02)00393-5

837